Dynamics of Drilling Systems With an Antistall Tool: Effect on Rate of Penetration and Mechanical Specific Energy

Thijs Vromen, ASML Netherlands B.V. and Eindhoven University of Technology; **Emmanuel Detournay,** University of Minnesota; **Henk Nijmeijer,** Eindhoven University of Technology; and **Nathan van de Wouw,** Eindhoven University of Technology, Delft University of Technology, and University of Minnesota

Summary

This paper considers the effect of an antistall tool on the dynamics of deep drilling systems. Field results show that the antistall tool increased the rate of penetration (ROP) of drilling systems when compared with ROP in offset wells drilled without this tool. We developed a model-based approach to investigate the effect of this downhole tool on the ROP and on the mechanical specific energy. Toward this, a drillstring model including the antistall tool was constructed; it describes the coupled axial/torsional dynamics in the form of delay differential equations. Simulation results and a dynamic analysis based on averaging the obtained steady-state response show that an increased drilling efficiency was obtained using the antistall tool, resulting in a higher ROP.

Introduction

This paper focuses on the role of the antistall tool (Haughom and Reimers 2006) to improve the drilling efficiency of polycrystalline-diamond-compact (PDC) bits. The antistall tool is a mechanical downhole tool that is placed in the bottomhole assembly (BHA). It consists of two tool bodies interconnected by a helical spline and an internal preloaded spring **(Fig. 1).** Under normal stable conditions, the tool transfers torque and weight to the bit as a passive part of the BHA. However, any abrupt change in torque, such as a torque spike from the cutters suddenly engaging a hard stringer, causes a telescopic contraction of the tool along an internal helix. An internal spring in the tool then gradually extends the tool as the torque-on-bit (TOB) decreases.

Akutsu et al. (2015) reported that the antistall tool improved drilling efficiency with PDC bits in terms of increased penetration rates and PDC-bit durability, especially in hard formations. Field results suggested that the incorporation of the antistall tool resulted in a higher drilling efficiency compared with that in offset wells, especially resulting in an increased surface ROP for similar operating conditions regarding the weight on bit (WOB) (Kjøglum 2007; Selnes et al. 2009; Reimers 2012, 2014; Akutsu 2015). Despite the evidence obtained from field data, a fundamental physics-based explanation for these effects is still lacking to this date.

The main objective of this work was to develop a modeling approach for a drillstring system that included an antistall tool (Selnes et al. 2009) and to perform analyses to investigate the working principle of the tool. In this context, the main contributions of this paper are as follows. First, a model of the drilling dynamics including a model of the tool was constructed. A key functional aspect of the antistall tool was the coupling of the axial and torsional dynamics of the drillstring; see Fig. 1. Therefore, we constructed a model of the drillstring dynamics that took into account both the axial and the torsional dynamics. The developments in this paper were based on the model presented by Besselink et al. (2011), which was an adapted version of the model proposed by Richard et al. (2007). This model, including extended versions and/or adaptations of the original model, was widely used for stability analysis of the drillstring dynamics (Germay et al. 2009a,b; Besselink et al. 2011; Liu et al. 2013; Nandakumar and Wiercigroch 2013; Depouhon and Detournay 2014; Aarsnes and Aamo 2016) and also for controller design (Besselink et al. 2015). Second, a simulation tool was developed to numerically obtain the response of the resulting nonlinear (nonsmooth) drillstring model with state-dependent delay. On the basis of the simulation results, the dynamic behavior of the key variables of the drillstring system, such as the WOB, TOB, and (bit) angular and axial velocities of the system, was investigated. Third, we performed dynamic analyses on the drillstring dynamics including the antistall tool and compared the results with a benchmark model without the tool to assess the effectiveness of the tool in improving ROP. This study of the effect of the antistall tool on the ROP and on the mechanical specific energy was performed on the basis of the average of the steady-state response of the nonlinear model. To the best of the authors' knowledge, these results were the first attempt to model the drillstring dynamics including the antistall tool and to analyze its main working principle and effectiveness.

The outline of this paper is as follows. First, the drillstring model including the antistall tool is introduced. The resulting nonlinear drillstring model with state-dependent delay was then used for a simulation study to analyze the effect of the antistall tool on the ROP. Finally, the main results of this work are summarized.

Modeling of the Drillstring Dynamics

We provided a concise overview of a benchmark drillstring model that describes the coupling of the axial and torsional dynamics, excluding the tool. The antistall tool was modeled, resulting in an extended drillstring model. Finally, a model reformulation was given to obtain a dimensionless model of the drillstring dynamics, which was used for the simulation studies in the following sections.

Modeling of the Benchmark Drillstring Dynamics. A rotary drilling system essentially consists of a rig on the surface and a drillstring that can be several kilometers in length, as shown in **Fig. 2.** The bottom part of the drillstring, known as the BHA, is made up of a drill collar equipped with downhole tools (e.g., downhole motors, stabilizers, and measurement-while-drilling tools) and a drill bit at its end.

Here, we represented the drillstring in the form of a discrete system, which is schematically depicted in **Fig. 3a.** The BHA was modeled as a point mass M with inertia I representing the first modal inertia of the combined drillpipe and BHA, while the drillpipe was

Original SPE manuscript received for review 15 March 2018. Revised manuscript received for review 27 August 2018. Paper (SPE 194487) peer approved 16 October 2018.

modeled as a spring with torsional stiffness C and axial stiffness K. The viscous friction along the drillpipe and the BHA was accounted for by the friction parameter D. This discrete representation of the drillstring embedded the low-frequency dynamics of the real system. This approach allowed us to gain insight into the effect of the tool on the averaged (i.e., slow time scale) ROP.[1]

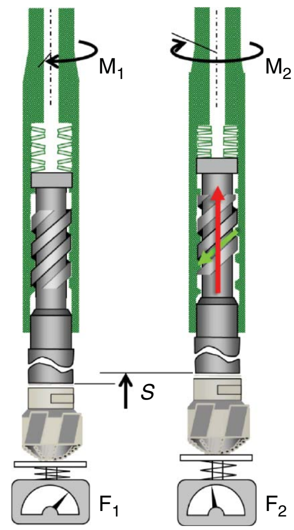

Fig. 1—Antistall tool. An increase in torque (M_2) will cause a telescopic contraction (S) (Akutsu et al. 2015).

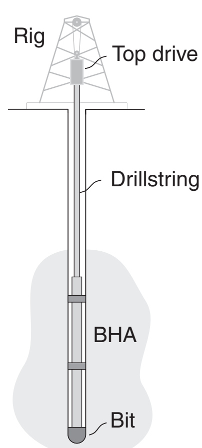

Fig. 2—Schematic of a drilling system for a vertical borehole configuration (Besselink et al. 2015).

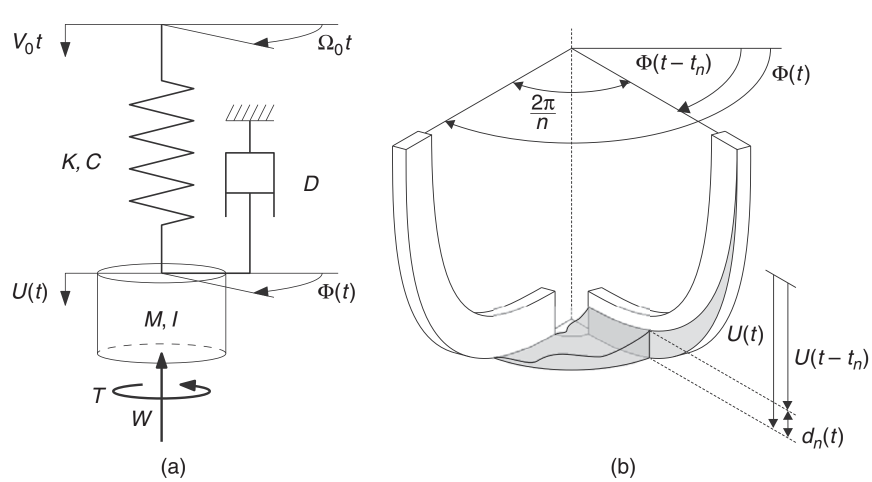

Fig. 3—(a) Schematic of a drillstring (Besselink et al. 2011) and (b) bottomhole profile between two successive blades of cutters (Richard et al. 2007).

[1]The model presented here can be extended to finite-element-method-based models or distributed drillstring models (Germay et al. 2009a; Aarsnes and Aamo 2016; Aarsnes and van de Wouw 2018).

Assuming that a constant angular velocity Ω_0 and a constant vertical velocity V_0 were imposed at the rig, the equations of motion characterizing the discrete system are

$$M\ddot{U} + D\dot{U} + K(U - V_0 t) = -W_c - W_f. \quad (1)$$

$$I\ddot{\Phi} + C(\Phi - \Omega_0 t) = -T_c - T_f. \quad (2)$$

Here, U denotes the axial position and Φ the angular position of the drill bit, while W_i and T_i ($i \in \{c, f\}$) denote, respectively, the axial force and torque on the drill bit resulting from the bit/rock interaction.

The axial force W and torque T acting on the bit reflect the existence of two independent processes: rock fragmentation in front of the cutters and frictional contact between the cutter wearflat and the rock. Hence, both W and T have a cutting and friction component, denoted by subscripts c and f, respectively (i.e., $W = W_c + W_f$ and $T = T_c + T_f$). Following Detournay and Defourny (1992) and Richard et al. (2007), these two processes are described as

$$W_c = na\zeta\varepsilon d_n, \quad W_f = na\ell_n\bar{\sigma}\frac{1 + \mathrm{Sign}(\dot{U})}{2} \quad (3)$$

$$T_c = \frac{1}{2}na^2\varepsilon d_n, \quad T_f = \frac{1}{2}na^2\xi\mu\ell_n\bar{\sigma}\frac{1 + \mathrm{Sign}(\dot{U})}{2}, \quad (4)$$

where a denotes the drill-bit radius and

$$\mathrm{Sign}(y) := \begin{cases} -1 & \text{for} \quad y < 0 \\ [-1, 1] & \text{for} \quad y = 0 \\ 1 & \text{for} \quad y > 0 \end{cases}$$

is the set-valued sign function. Eqs. 3 and 4 assume that the bit consists of n symmetrically positioned full blades.

Considering the cutting process, Eqs. 3 and 4 indicate that the cutting forces acting on a blade are proportional to the depth of cut (DOC) d_n, which corresponds to the height of the rock step in front of a single blade. The factors of proportionality contain the intrinsic specific energy ε, which represents the energy required to destroy a unit volume of rock, and the number ζ, which is related to the orientation of the cutting force on the blade. The DOC d_n generally evolves with time. It depends on the axial position of the blade with respect to the rock surface that was generated by the previous blade at time $t - t_n$; see Fig. 3b. The time-dependent delay $t_n(t)$ represents the time interval it takes for the bit to rotate $2\pi/n$ rad, which is the angle between two successive blades on the bit:

$$\int_{t-t_n(t)}^{t} \frac{\mathrm{d}\Phi(s)}{\mathrm{d}s}\mathrm{d}s = \Phi(t) - \Phi[t - t_n(t)] = \frac{2\pi}{n}. \quad (5)$$

Eq. 5 expresses the fact that the delay depends on the rotational response of the system. The delay is, thus, state-dependent and is affected by the presence of the antistall tool in the BHA, because the tool influenced the state response. Hence, $d_n(t)$ can be expressed as

$$d_n(t) = U(t) - U[t - t_n(t)]. \quad (6)$$

Lateral motions of the drill bit (i.e., bit whirl) were not considered, and it was assumed that the drill bit moved down in a perfectly vertical well in the calculation of the DOC $d_n(t)$ and the delay $t_n(t)$.

The frictional process takes place at the interface between cutter wearflat and the rock. It is described by four parameters: (i) ℓ_n, the length of the wearflat on a blade (in the direction orthogonal to the blade)—assumed to be uniform; (ii) $\bar{\sigma}$, the contact strength representing the maximum contact stress on the wearflat; (iii) the friction coefficient μ; and (iv) the number ξ, characterizing the spatial distribution of the wearflats. Saturation of the normal stress acting on the wearflat reflects the existence of a plastic flow mechanism in the rock beneath the cutter (Zhou and Detournay 2014). According to experimental evidence (Detournay et al. 2008), the contact forces do saturate when the bit moves downward into the rock. On the other hand, the contact forces vanish when the bit moves upward, because the wearflats are no longer in contact with the rock. Accordingly, the contact WOB W_f in Eq. 3 is modeled using the sign function. The set-valued nature of this sign function implies that W_f can take any value between zero and its saturation value $n\ell_n a\sigma$, when the bit axial velocity vanishes; actual value being dictated by equilibrium consideration. The frictional torque T_f is related to W_f through the friction coefficient μ and the number ξ.

Eqs. 1 through 5 describe the model used as a benchmark to compare with the model that includes the antistall tool presented next.

Modeling of the Drillstring Dynamics Including the Antistall Tool. The antistall tool consists of two tool bodies interconnected by a helical spline and an internal preloaded spring, as illustrated in **Fig. 4a.** A torque of large enough magnitude to overcome the effect of the preload causes a rotation of the upper tool part with the internal helical spline relative to the mating lower part and, thus, a contraction of the tool (Selnes et al. 2009).

The model presented in the previous subsection was then extended to include the downhole tool. A schematic of the drilling structure including the tool is shown in Fig. 4b. Now, the BHA is composed of two parts. The upper component is modeled as a discrete mass M with inertia I and again represents the first modal inertia of the combined drillpipe and the part of the BHA above the tool. The lower component represents the part of the BHA below the tool and was modeled as a mass M_b with inertia I_b. Let U and Φ, respectively, denote the axial and angular position of the BHA (above the antistall tool), and U_b and Φ_b the axial and angular position of the bit (i.e., below the tool). The generalized coordinates describing the system are given by $q = [U, U_b, \Phi, \Phi_b]^T$. The forces W and torques T now depend additionally on U, $\dot{U}$, and Φ, as seen in Fig. 4b. The antistall tool was modeled by adding an axial spring K_b and an axial damper D_b and by introducing a kinematic constraint to describe the coupling between the axial and angular displacement, imposed by the helical spline of the tool. The holonomic constraint equation results from the relation between the lead p, lead angle β, and the pitch radius r:

$$U - U_b = \frac{p}{2\pi r}(\Phi r - \Phi_b r) = \frac{p}{2\pi}(\Phi - \Phi_b) =: \alpha(\Phi - \Phi_b). \quad (7)$$

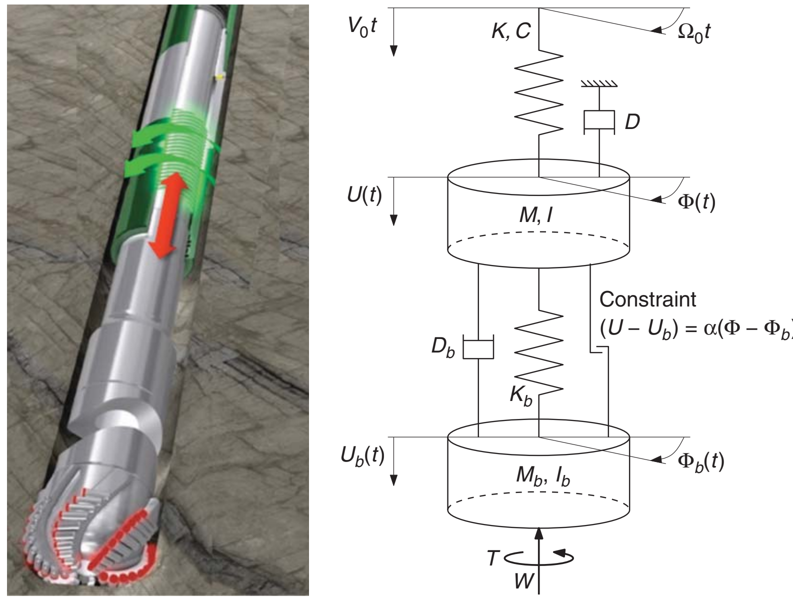

(a) (b)

Fig. 4—(a) Impression of the working principle of the antistall tool (Tomax AS) and (b) schematic of a drillstring including the antistall tool.

The equations of motion for this system are then derived by adopting a Lagrangian approach for systems with constraints,

$$\begin{aligned}
&M\ddot{U} + D\dot{U} + D_b(\dot{U} - \dot{U}_b) + K(U - V_0 t) + K_b(U - U_b) = -\Lambda \\
&M_b\ddot{U}_b - D_b(\dot{U} - \dot{U}_b) - K_b(U - U_b) = -W_c - W_f + \Lambda \\
&I\ddot{\Phi} + C(\Phi - \Omega_0 t) = \alpha\Lambda \\
&I_b\ddot{\Phi}_b = -T_c - T_f - \alpha\Lambda,
\end{aligned} \tag{8}$$

where Λ is the associated Lagrange multiplier. From the constraint depicted in Eq. 7, it follows that

$$\begin{aligned}
&\Phi = \frac{U - U_b}{\alpha} + \Phi_b \\
&\ddot{\Phi} = \ddot{U} - \frac{\ddot{U}_b}{\alpha} + \ddot{\Phi}_b,
\end{aligned} \tag{9}$$

which is used in the third line of Eq. 8 to obtain

$$I\left(\frac{\ddot{U} - \ddot{U}_b}{\alpha} + \ddot{\Phi}_b\right) + C\left(\frac{U - U_b}{\alpha} + \Phi_b - \Omega_0 t\right) = \alpha\Lambda. \tag{10}$$

Hence, λ satisfies

$$\Lambda = \frac{I}{\alpha}\left(\frac{\ddot{U} - \ddot{U}_b}{\alpha} + \ddot{\Phi}_b\right) + \frac{C}{\alpha}\left(\frac{U - U_b}{\alpha} + \Phi_b - \Omega_0 t\right). \tag{11}$$

The degree of freedom related to Φ can then be eliminated from Eq. 8 by using Eq. 11. The expressions for the force, torque, DOC, and time-dependent delay are similar to those derived for the benchmark model (see Eqs. 3 through 6), except that the displacements and velocities that play a role in the bit/rock interaction now appear as U_b, Φ_b, and $\dot{U}_b$, $\dot{\Phi}_b$. The resulting equations of motion in terms of U, U_b, and Φ_b (i.e., after elimination of the holonomic constraint in Eq. 7) are given by

$$\left(M + \frac{I}{\alpha^2}\right)\ddot{U} - \frac{I}{\alpha^2}\ddot{U}_b + \frac{I}{\alpha}\ddot{\Phi}_b + D\dot{U} + D_b(\dot{U} - \dot{U}_b) + K(U - V_0 t) + K_b(U - U_b) + \frac{C}{\alpha^2}(U - U_b) + \frac{C}{\alpha}(\Phi_b - \Omega_0 t) = 0. \tag{12}$$

$$\begin{aligned}
&-\frac{I}{\alpha^2}\ddot{U} + \left(M_b + \frac{I}{\alpha^2}\right)\ddot{U}_b - \frac{I}{\alpha}\ddot{\Phi}_b - D_b(\dot{U} - \dot{U}_b) - K_b(U - U_b) - \frac{C}{\alpha^2}(U - U_b) - \frac{C}{\alpha}(\Phi_b - \Omega_0 t) \\
&\quad = -na\zeta\varepsilon\{U_b(t) - U_b[t - t_n(t)]\} - na\ell_n\bar{\sigma}\,\frac{1 + \mathrm{Sign}(\dot{U}_b)}{2}.
\end{aligned} \tag{13}$$

$$\frac{I}{\alpha}\ddot{U} - \frac{I}{\alpha}\ddot{U}_b + (I_b + I)\ddot{\Phi}_b + \frac{C}{\alpha}(U - U_b) + C(\Phi_b - \Omega_0 t) = -\frac{1}{2}na^2\varepsilon\{U_b(t) - U_b[t - t_n(t)]\} - \frac{1}{2}na^2\xi\mu\ell_n\bar{\sigma}\,\frac{1 + \mathrm{Sign}(\dot{U}_b)}{2}. \tag{14}$$

The time-delay equation for the model with the antistall tool is

$$\int_{t - t_n(t)}^{t} \frac{\mathrm{d}\Phi_b(s)}{\mathrm{d}s}\mathrm{d}s = \Phi_b(t) - \Phi_b[t - t_n(t)] = \frac{2\pi}{n}. \tag{15}$$

This model can be used to analyze the effect of the downhole tool on the drilling dynamics and, in particular, on the ROP. However, the model was first formulated in a dimensionless form to reduce the number of parameters and to facilitate numerical analysis.

Model Reformulation. The equations of motion (Eqs. 12 through 15) were scaled to reduce the number of parameters, and, in addition, perturbation coordinates were introduced to describe the equations of motion around the nominal solution (corresponding to a constant rotational speed and constant ROP, thereby reflecting nominal drilling conditions). We then introduced the characteristic time and length as $t_* = \sqrt{\frac{I}{C}}$, $L_* = \frac{2C}{\varepsilon a^2}$.

Typically, $t \approx 1$ sec and $L \approx 1$ mm. These characteristic parameters are used to denote coordinate transformation:

$$u(\tau) = \frac{U - U_0}{L_*}, \quad u_b(\tau) = \frac{U_b - U_{b0}}{L_*}, \quad \varphi_b(\tau) = \Phi_b - \Phi_{b0}, \tag{16}$$

where u, u_b, and φ_b are functions of the dimensionless time

$$\tau = \frac{t}{t_*} \tag{17}$$

and represent the (scaled) relative axial (u and u_b) and torsional (φ_b) displacements. In Eq. 16, $U_0(t)$, $U_{b0}(t)$, and $\Phi_{b0}(t)$ are the nominal solutions of Eqs. 12 through 14, which are given by

$$\begin{aligned} U_0 &= V_0 t - \frac{DV_0 + B}{K} \\ U_{b0} &= V_0 t - \frac{DV_0}{K} - \frac{A}{\alpha K_b} - \frac{B(K + K_b)}{K_b K} \\ \Phi_{b0} &= \Omega_0 t - \frac{A}{\alpha^2 K_b} - \frac{A}{C} - \frac{B}{\alpha K_b}, \end{aligned} \tag{18}$$

with $A := \frac{1}{2} n a^2 \varepsilon V_0 t_{n0} + \frac{1}{2} n a^2 \xi \mu \ell_n \bar{\sigma}$ and $B := n a \zeta \varepsilon V_0 t_{n0} + n a \ell_n \bar{\sigma}$. These solutions correspond to a constant axial and torsional velocity V_0 and Ω_0, respectively, and also induce a constant delay $t_{n0} = \frac{2\pi}{\Omega_0 n}$. In dimensionless time, the time delay is given by $\tau_n = \frac{t_n}{t_*}$ and the prescribed velocities at the surface in their dimensionless form are given by

$$v_0 = \frac{V_0 t_*}{L_*}, \quad \omega_0 = \Omega_0 t_*. \tag{19}$$

In addition, a perturbation of the time delay with respect to the nominal time delay was introduced:

$$\hat{\tau}_n = \tau_n - \tau_{n0}, \tag{20}$$

where $\tau_{n0} = \frac{t_{n0}}{t_*} = \frac{2\pi}{\omega_0 n}$. The above scaling and introduction of perturbation coordinates led to the following dimensionless model formulation:

$$(1 + \kappa)u'' - \kappa u_b'' + \nu \varphi_b'' + \gamma u' - \gamma_b(u_b' - u') + \eta^2 u + \eta_b^2(u - u_b) + \kappa(u - u_b) + \nu \varphi_b = 0 \tag{21}$$

$$-\kappa u'' + (m_* + \kappa)u_b'' - \nu \varphi_b'' + \gamma_b(u_b' - u') - \eta_b^2(u - u_b) - \kappa(u - u_b) - \nu \varphi_b = n\psi[-u_b(\tau) + u_b(\tau - \tau_n) - v_0 \hat{\tau}_n + \lambda_n g(u_b')] \tag{22}$$

$$(1 + \iota)\varphi_b'' + \varphi_b + \frac{\kappa}{\nu} u'' - \frac{\kappa}{\nu} u_b'' + \frac{\kappa}{\nu}(u - u_b) = n\left[-u_b(\tau) + u_b(\tau - \tau_n) - v_0 \hat{\tau}_n + \beta \lambda_n g(u_b')\right] \tag{23}$$

$$\varphi_b(\tau) - \varphi_b(\tau - \tau_n) + \omega_0 \hat{\tau}_n = 0, \tag{24}$$

where the prime $(\cdot)'$ denotes differentiation with respect to the dimensionless time τ. The dimensionless DOC is given by

$$\delta = u_b(\tau) - u_b(\tau - \tau_n) + v_0 \tau_n, \tag{25}$$

and perturbations, with respect to the nominal DOC, were defined as $\hat{\delta} := \delta - \delta_0$ with $\delta_0 = \frac{2\pi v_0}{n \omega_0} = v_0 \tau_{n0}$. The parameters used in this dimensionless form are given in **Table 1** with the corresponding physical parameters of the drilling system listed in Appendix B.

The nonlinear function $g(u_b')$ in Eqs. 22 and 23 describes whether the wearflat was in contact with the rock ($g = 0$) or not ($g = 1$), whereas the discontinuity at $u_b' = -v_0$ is represented by a convex set-valued map:

$$g(u_b') \in \frac{1 - \mathrm{Sign}(u_b' + v_0)}{2} = \begin{cases} 0, & u_b' > -v_0 \\ [0, 1], & u_b' = -v_0 \\ 1, & u_b' < -v_0, \end{cases} \tag{26}$$

where $\mathrm{Sign}(\cdot)$ is the set-valued sign function. Hence, the model in Eqs. 21 through 24 and the set-valued map in Eq. 26 constitute a delay-differential inclusion with state-dependent delay, describing the drillstring dynamics in perturbation coordinates.

It has to be noted that the model presented in Eqs. 21 through 24 describes the dynamics for nonnegative DOC ($d \geq 0$, i.e., $\delta \geq 0$) and positive angular velocity of the bit ($\varphi_b' > -\omega_0$, which corresponds to $\dot{\Phi} > 0$). This means that the model loses validity when the

DOC becomes negative as a result of severe axial vibrations (i.e., bit bouncing) or when the bit is sticking in the torsional direction. Nonetheless, the model can be used to predict the onset of torsional vibrations that can lead to stick/slip. An approach for the inclusion of torsional stick in the model was given by Besselink et al. (2011) and was also used for the simulation results in the next section.

Parameter	Symbol	Value
Drillstring design	$\psi = \dfrac{\zeta \varepsilon a l}{MC}$	129.4
Drill-bit design	$\beta = \zeta \mu \xi$	0.36
Wearflat friction	$\lambda_n = \dfrac{a^2 \ell_n \bar{\sigma}}{2\zeta C}$	5.6
Scaled viscous friction	$\eta = \sqrt{\dfrac{K_p I}{MC}}$	1.59
Scaled axial damping	$\gamma = \dfrac{D}{M}\sqrt{\dfrac{I}{C}}$	0.86
Scaled viscous friction in antistall tool	$\eta_b = \sqrt{\dfrac{K_{AST} I}{MC}}$	4.62
Scaled axial damping in antistall tool	$\gamma_b = \dfrac{D_{AST}}{M}\sqrt{\dfrac{I}{C}}$	0.18
Mass ratio	$m_* = M_b/M$	0.080
Inertia ratio	$\iota = I_b/I$	0.082
Scaled inertia	$\kappa = \dfrac{I}{M\alpha^2}$	0.94
Scaled lead antistall tool	$\nu = \dfrac{k\alpha}{L_*}$	213.0

Table 1—Parameters of the drillstring model including the antistall tool in dimensionless form (Eqs. 21 through 24).

Effect of the Tool on the Drillstring Dynamics

The effect of the tool on the drillstring dynamics was investigated, focusing on the axial response characteristics, as discussed in the next section, because these ultimately determine the ROP and the associated (average) WOB needed to generate this ROP. A more detailed investigation of the effect of the tool on the ROP is given in a subsequent section.

Axial Response Characteristics. Simulation results of the drillstring models with and without the antistall tool were calculated. For these simulations, we used a dedicated simulation environment that was developed to numerically obtain the response of the dynamic drillstring model with set-valued discontinuity and state-dependent delay. Toward this, we used the models in perturbation coordinates, as presented in a previous section, for the drillstring model with and without the antistall tool. However, the results were presented in the system coordinates $q = [U, U_b, \Phi, \Phi_b]^T$ to support straightforward physical interpretation of the results.

The model results, with and without the downhole tool, were presented for two different operating scenarios: a "low"-rotary-speed case, where $\Omega_0 = 50$ rev/min, and a "high"-rotary-speed case, where $\Omega_0 = 120$ rev/min. The prescribed axial velocity at the topdrive was considered equal to $V_0 = 20$ ft/hr for both scenarios. These two scenarios were chosen because they reflect nominal drilling operations, and field observations that show the tool performance might depend on the rotary speed, which was investigated by comparing the results of the two scenarios. Moreover, by considering both low- and high-rotary-speed cases, we assessed whether the tool was effective over a broad range of operating conditions. In analyzing the results of the simulations, the focus was on the axial response of the drilling system, because it was the axial motion of the bit that determined the ROP.

The simulation result for the first operating scenario of the benchmark model is shown in **Fig. 5a and 5b** (top two plots) in terms of the axial bit velocity $\dot{U}$ (Fig. 5a) and the corresponding total WOB $W = W_f + W_c$ (Fig. 5b). The initial conditions of the system coordinates were chosen close to the desired set point; small initial perturbations with respect to the nominal solution corresponding to a constant rotational velocity and constant ROP were used. After the occurrence of some transient oscillations in approximately the first 80 seconds, the response converged to an axial stick/slip limit cycle. This vibrational behavior was caused by an axial instability of the nominal solution, which was shown to be present for almost all realistic operational drilling scenarios (Besselink et al. 2011; Depouphon and Detournay 2014).

To study the response of the drillstring model, including the antistall tool, the simulations were performed under the same operating conditions as the simulation for the benchmark model. The response of the system with a desired rotary speed of 50 rev/min is shown in Fig. 5c and 5d. In this figure, the axial velocity of the bit $\dot{U}_b$ (Fig. 5c) and the corresponding total WOB $W = W_f + W_c$ (Fig. 5d) are shown. The system also converged to an axial stick/slip limit cycle, which significantly differed from the axial limit cycle for the benchmark model. In particular, we observed that the amplitude of the axial vibrations at the bit increased, with peak values up to 5X the amplitude of the axial vibrations in the simulation of the benchmark model. Given the fact that the axial velocity of the topdrive was an imposed boundary condition in both models, the average axial velocity (expressed as ROP) was the same for both models by definition. However, the essential difference in the axial response became even more apparent when the WOB ($W = W_f + W_c$) response was compared (see Figs. 5b and 5d). These figures show that the WOB response was significantly changed by the downhole tool (for the same ROP); in particular, the WOB was (on average) lower for the system with the tool. Further insights regarding this fact will be discussed in a later section.

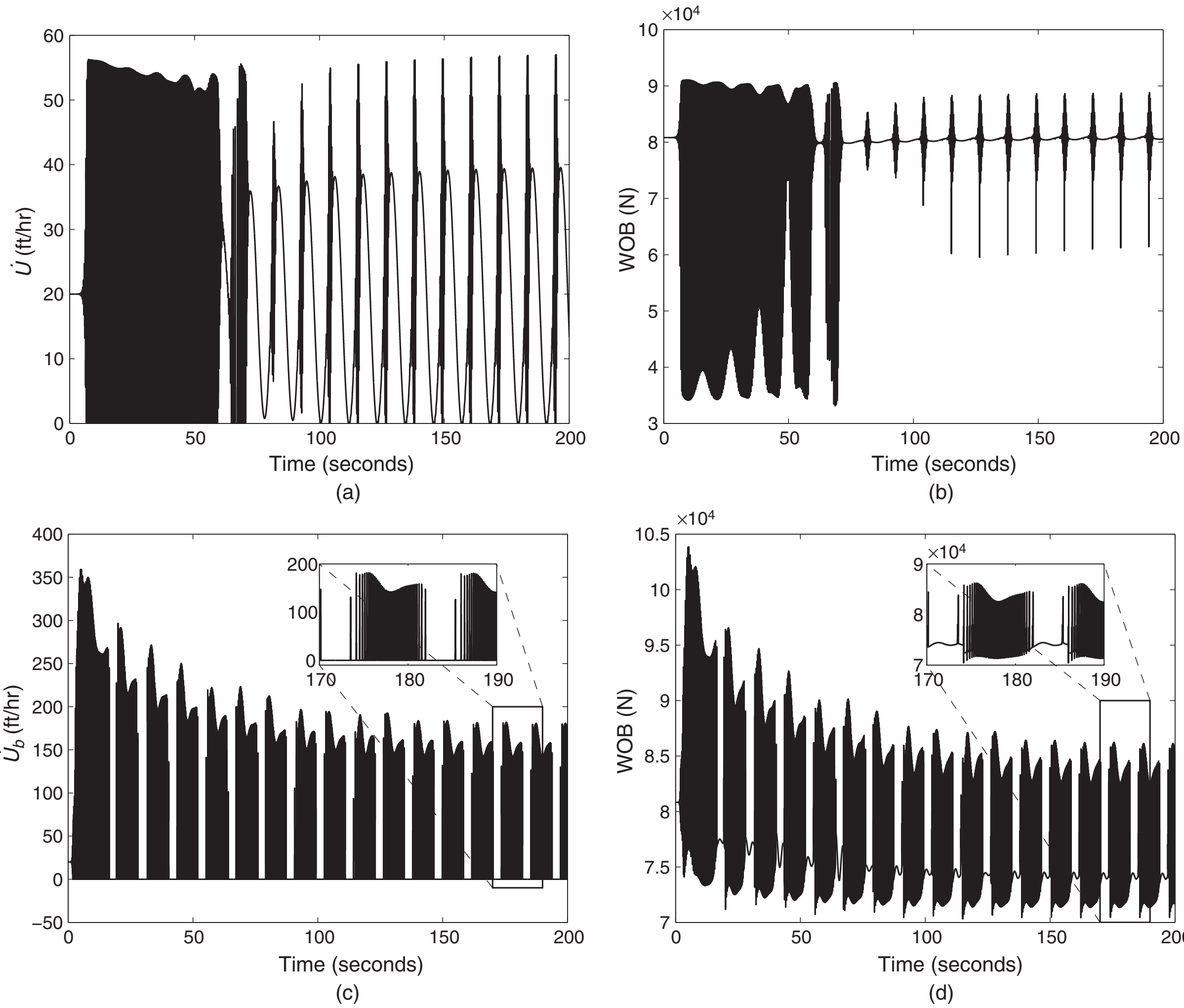

Fig. 5—Comparison of simulation results between benchmark model (BM) and model with an antistall tool (AST) for a prescribed rotary speed of 50 rev/min and axial velocity of 20 ft/hr: (a) axial bit velocity (BM), (b) WOB (BM), (c) axial bit velocity (AST), (d) WOB (AST).

The results of the second scenario, with a desired rotary speed of 120 rev/min, are shown in **Fig. 6** for the benchmark model (Figs. 6a and 6b) and the model including the tool (Figs. 6c and 6d). The axial vibrations were lower in amplitude for the 120-rev/min case compared to the 50-rev/min case. Moreover, a comparison of Figs. 6b and 6d shows that the WOB response was significantly changed by the downhole tool (for the same ROP).

Effect of the Tool on the ROP. Here, we investigated the claim that the presence of the tool in the BHA resulted in an increase of performance, under otherwise identical conditions. Since the axial velocity was imposed as a surface boundary condition in the model, improvement of drilling efficiency attributable to the antistall tool was assessed by comparing the average WOB predicted by the benchmark model with the model that includes the antistall tool for the same prescribed axial velocities at the topdrive; a decrease of the average WOB then translated into an increase of drilling efficiency. The dynamic response of the model was meaningfully averaged, in particular the cutting force W_c and contact force W_f, when the system reached a steady-state limit cycle (generally an axial stick/slip limit cycle for most parameter settings). Thus, under steady-state conditions, the total average WOB W was calculated as a function of the average penetration rate of the bit, which was evidently equal to the prescribed axial velocity at the surface, noting, however, that oscillations of the bit axial velocity occurred as a result of the drillstring dynamics.

The results of the averaged total WOB W for both models are shown in **Figs. 7a and 7b,** for $\Omega_0 = 50$ rev/min and $\Omega_0 = 120$ rev/min, respectively. These figures show that, to achieve the same ROP, a lower WOB is required for the system with the tool or equivalently that a higher ROP is reached for a given average WOB, for the system with the tool. For example, for a rotary speed of $\Omega_0 = 50$ rev/min, an averaged WOB of 75 kN resulted in an averaged ROP of 10 ft/hr for the benchmark model, and approximately 22.9 ft/hr for the model including the antistall tool, corresponding to an increase of more than 100% (see the dashed lines in Fig. 7a). In the case of $\Omega_0 = 120$ rev/min and an averaged WOB of 75 kN, the ROP was approximately 15.7 ft/hr for the benchmark model and 23.8 ft/hr for the model with the antistall tool, again an increase of approximately 50% (Fig. 7b).

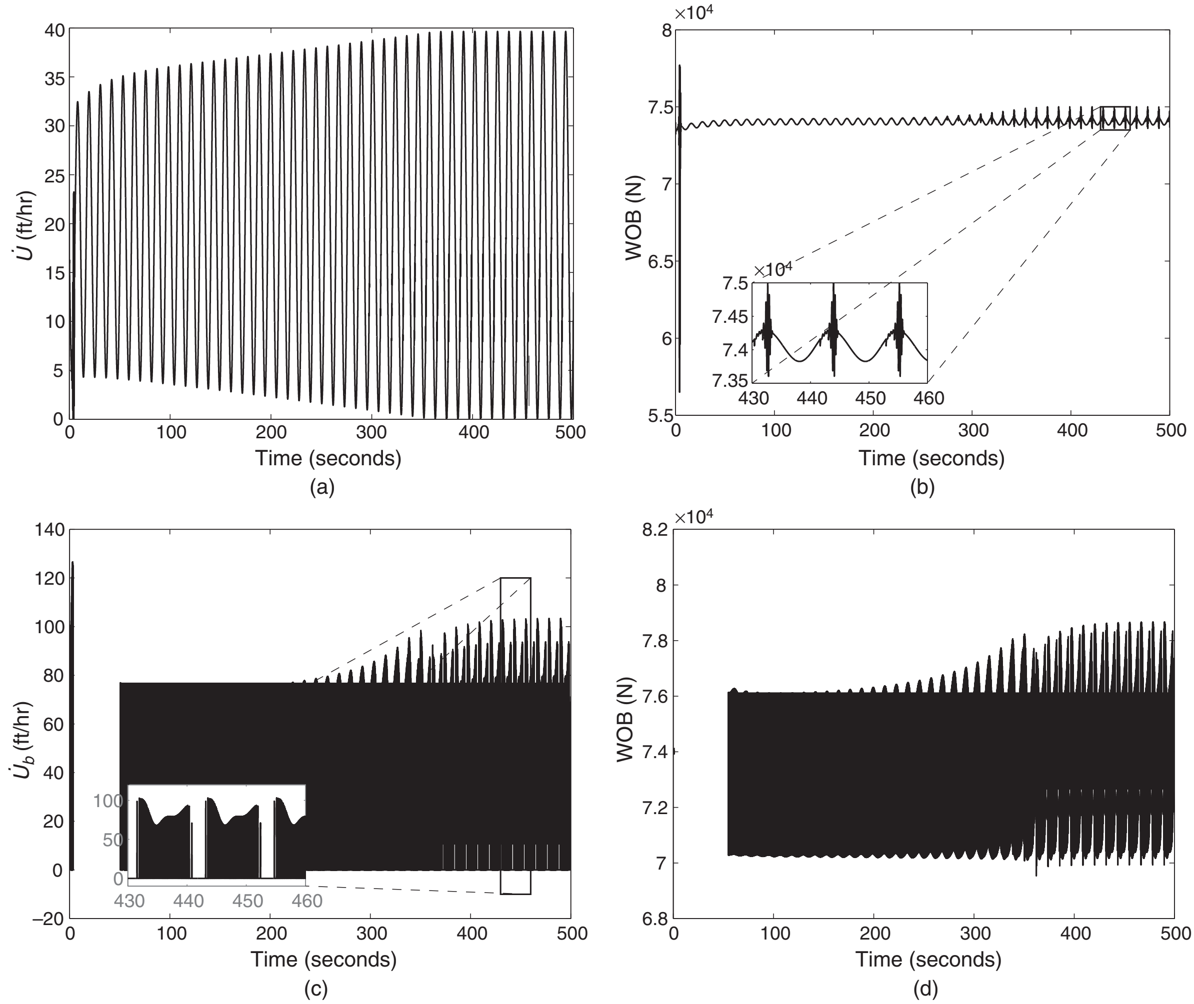

Fig. 6—Comparison of simulation results between benchmark model (BM) and model with an antistall tool (AST) for a prescribed rotary speed of 120 rev/min and axial velocity of 20 ft/hr: (a) axial bit velocity (BM), (b) WOB (BM), (c) axial bit velocity (AST), (d) WOB (AST). The initial conditions for this scenario were chosen relatively far from the desired set point because of the slow growth rate of the oscillations toward the steady-state limit cycle.

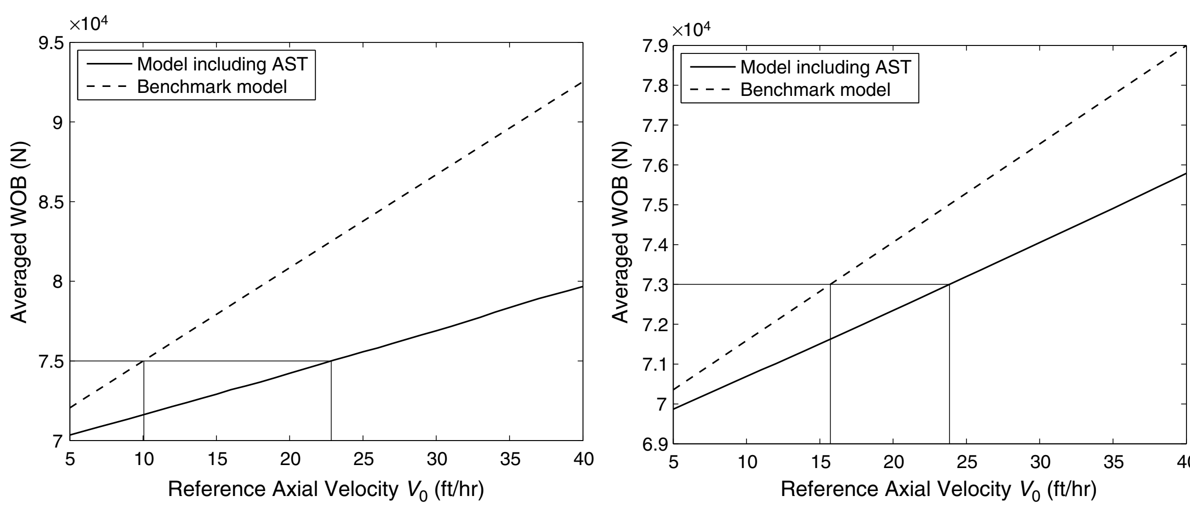

Fig. 7—Averaged value of the total WOB as function of the prescribed axial velocity at the top of the drillstring: (a) with a prescribed rotational velocity of 50 rev/min and (b) with a prescribed rotational velocity of 120 rev/min.

To further investigate the mechanism behind the improved drilling efficiency with the antistall tool, we separately analyzed the dependence of the cutting and contact components of the averaged WOB on the average ROP (see **Figs. 8a and 8b**) for the 50-rev/min and 120-rev/min cases, respectively. According to the expression for the contact force given in Eq. 3, W_f can vary between zero and the maximum value of $na\ell_n\bar{\sigma}$ when the bit was in axial stick—i.e., when $\dot{U}_b = 0$ ($\dot{U} = 0$ for the benchmark model). On the other hand, the wearflat force was always this maximum value $na\ell_n\bar{\sigma}$ when the bit was in axial slip—i.e., when $\dot{U}_b > 0$ ($\dot{U} > 0$ for the benchmark model). In fact, it can be observed in Fig. 8 that, for all axial velocities, the averaged contact force $\langle W_f \rangle$ of the benchmark model was equal to (or at least close to) this maximum value of $na\ell_n\bar{\sigma} = 69.12$ kN (six-blade bit, $n = 6$, radius of the bit $a = 0.16$ m (12.25 in.), wearflat length $\ell_n = 1.2$ mm, contact stress $\bar{\sigma} = 60 \times 10^6$ Pa). Furthermore, the response of the contact force W_f as a function of time for the case of 120 rev/min shown in **Fig. 9a,** indicated that the maximum wearflat force $na\ell_n\bar{\sigma} = 69.12$ kN was almost activated everywhere for the benchmark model; even when $\dot{U} = 0$ (i.e., the bit was sticking in the axial direction), W_f is close to the maximum value.

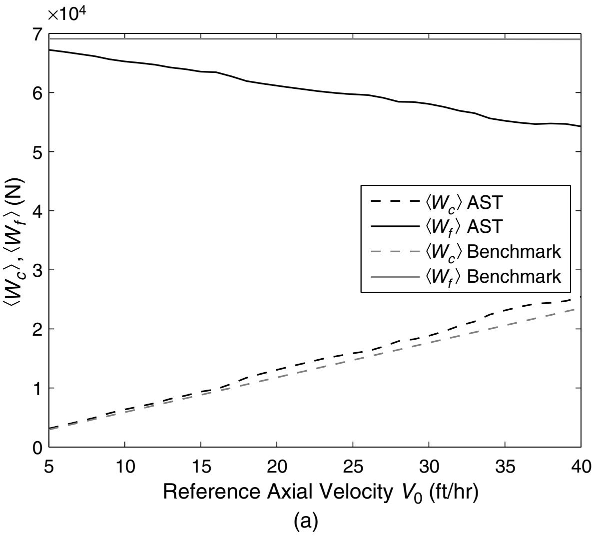

Fig. 8—Averaged value of the cutting force $\langle W_c \rangle$ and frictional contact force $\langle W_f \rangle$ as result of averaging the response of drillstring dynamics: (a) for a prescribed rotational velocity of 50 rev/min and (b) for prescribed rotational velocity of 120 rev/min.

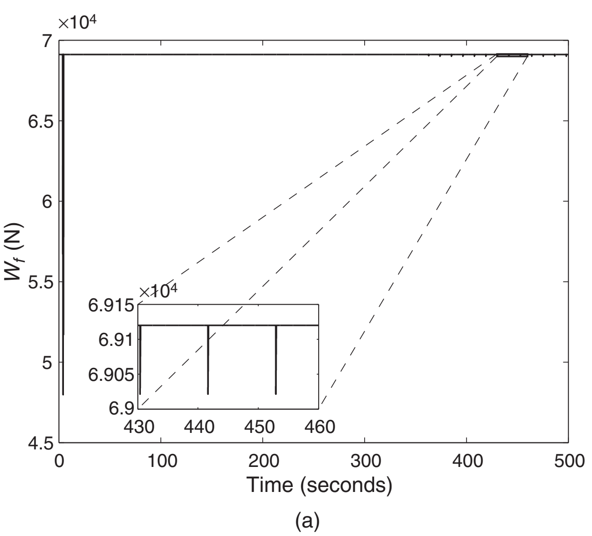

Fig. 9—Time response of the wearflat force W_f for a rotary speed of 120 rev/min and V_0 = 20 ft/hr: (a) for the benchmark model and (b) for the model with tool.

For the model with the antistall tool, the averaged contact force $\langle W_f \rangle$ was decreasing during increasing axial velocity V_0 (see Fig. 8b). In addition, the averaged wearflat force was up to 10% (depending on V_0) lower than the saturation $na\ell_n\bar{\sigma}$. The time response of the wearflat force showed that, during axial stick phases, W_f was reduced for the system with the tool (see Fig. 9b). This implied that the antistall tool contracted during axial stick, thus reducing the wearflat force. Moreover, the average cutting force increased for the model with the antistall tool in comparison with the benchmark model; see Fig. 8b for the case of 120 rev/min. The time variation of the cutting force, for 120 rev/min and $V_0 = 20$ ft/hr, is illustrated in **Fig. 10** for both models. This figure confirms that the cutting force was larger for the model with the tool. The simultaneous decrease of the contact force and increase of the cutting force resulting from the presence of the antistall tool in the BHA combined to improve the drilling efficiency. Thus, the presence of the antistall tool in the BHA actually made the axial dynamics more unstable, hence increasing the number of axial stick/slip events that were responsible for diverting a larger fraction of WOB to the cutting process because of a reduction in the component of WOB transmitted by the bit wearflats and chamfers. This mechanism suggested by our model explains the increased ROP observed in drilling operations with a BHA equipped with an antistall tool. Similar results were obtained during a rotary speed of 50 rev/min. In this case, the averaged contact force decreased even more during an increasing average penetration rate—up to 20% lower than the maximum value.

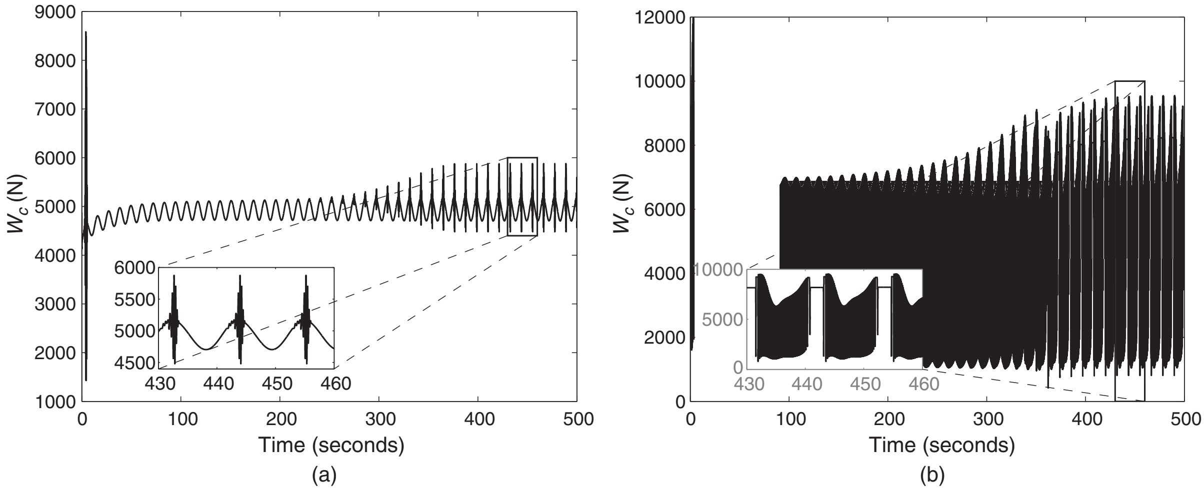

Fig. 10—Time response of the cutting force W_c for a rotary speed of 120 rev/min and $V_0 = 20$ ft/hr: (a) for the benchmark model and (b) for the model with tool.

Effect of the Tool on the Mechanical Specific Energy. The effect of the tool on the drilling efficiency was also analyzed from the point of view of the mechanical specific energy (Dupriest and Koederitz 2005). To do so, it was convenient to cast the averaged results in the *E-S* diagram used by Detournay and Defourny (1992) and Detournay et al. (2008). Noting that the TOB *T* and WOB *W* consisted of both a cutting and a contact component, and that the cutting component was proportional to the depth of cut per revolution *d* while the contact components were related through a friction law (see Eqs. 3 and 4), it was established that *T, W,* and *d* were necessarily constrained by

$$\frac{2T}{a} = (1 - \mu\xi\zeta)\varepsilon and + \mu\xi W. \qquad (27)$$

Upon dividing the product by the bit radius *a* with the depth of cut *nd,* Eq. 27 can be rewritten as (Detournay and Defourny 1992)

$$E = (1 - \beta)\varepsilon + \mu\xi S, \quad E \geq \varepsilon, \qquad (28)$$

where $E = 2T/a^2nd$ is the mechanical specific energy, $S = W/and$ is the drilling strength, and $\beta = \mu\xi\zeta$ is a number typically less than unity. While ε quantifies the specific energy associated with cutting only, *E* reflects dissipation in cutting and frictional contact. Thus, $E - \varepsilon$ represents the specific energy wasted by friction between the cutter wearflat and the rock and is ultimately transformed into heat. Alternatively, efficiency $\eta = \varepsilon/E$ quantifies the fraction of the energy supplied to the bit that was used to fragment and remove rock. In contrast, when ε was assumed to be independent of *d, E* increased with a decreasing depth of cut *d*. In other words, η increased with *d* under otherwise identical conditions.

The linear constraint shown in Eq. 28 is represented in the *E-S* diagram shown in **Fig. 11a.** Increasing forces transmitted by the wearflat surfaces of the bit caused the state point to move away from the cutting point, which represented the state of an ideally sharp bit.

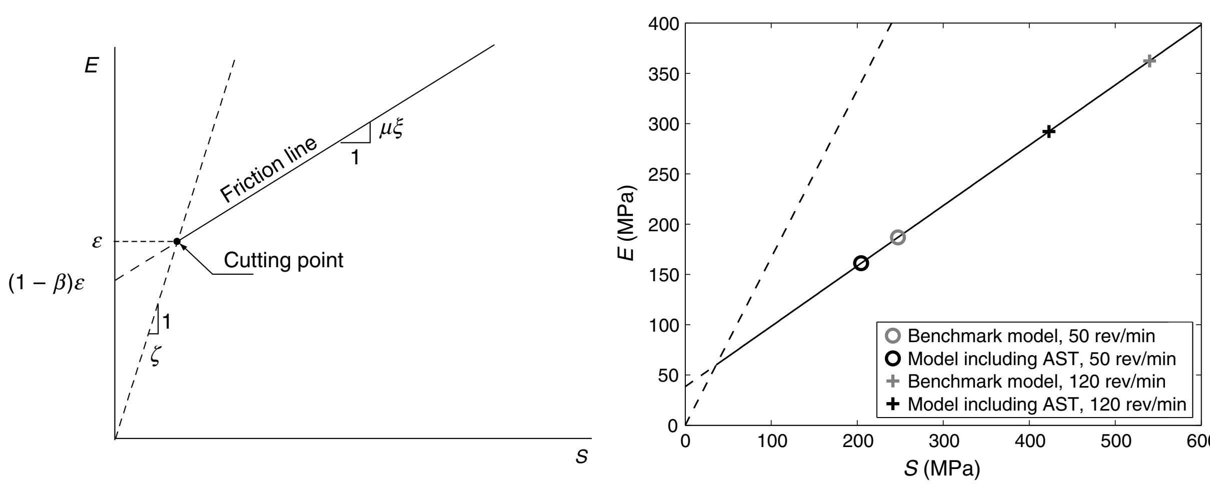

Fig. 11—*E-S* diagram: (a) the state point for a blunt bit lies on the friction line $E = (1 - \beta)\varepsilon + \mu\xi$. For an ideally sharp bit, the state point is on the cutting point; (b) results of simulations with and without the antistall tool.

As discussed previously, the increasing axial vibrations associated with the presence of the tool in the BHA caused, on average, a decrease of the contact forces and, thus, a decrease in the mechanical specific energy E. Fig. 11b illustrates the increase in drilling efficiency with the antistall tool, also summarized in **Table 2.** The simulations for 120 rev/min indicated higher specific energies compared with 50 rev/min. This increase was as a result of a smaller average depth of cut at 120 rev/min compared to 50 rev/min, because the average ROP was imposed as 20 ft/hr in all the simulations.

Model	rev/min	Efficiency η
Benchmark	50	0.321
Benchmark	120	0.166
AST	50	0.372
AST	120	0.205

Table 2—Results of simulations. AST = antistall tool.

To summarize, the preceding analysis of the effect of the antistall tool on the mechanical specific energy further explained why the tool improved the drilling efficiency and the ROP.

Discussion

In this work, the drillstring dynamics of a system including a downhole tool were analyzed. Although field results showed that the antistall tool increased the ROP when compared with ROP in offset wells, a fundamental physics-based explanation for these effects was currently lacking. Therefore, the drillstring dynamics of a system with an antistall tool were investigated in this research using a model-based approach.

A drillstring model including the antistall tool was constructed, including the coupled axial/torsional dynamics of the drillstring, a bit/rock interaction law, and a model of the tool. This model was formulated as a nonlinear (nonsmooth) delay-differential equation with state-dependent delay. In a simulation study, the axial response of this model was compared with a benchmark model of the drillstring dynamics without an antistall tool. The simulation results showed an unstable response of the drillstring dynamics for both the benchmark model and the model with the antistall tool, resulting in axial (stick/slip) limit cycles.

To investigate the claim regarding the increased ROP of the system including the antistall tool, the (averaged) WOB of the response of the nonlinear drillstring dynamics was analyzed. It showed that the benchmark model required a higher WOB to obtain the same ROP as the drillstring model including an antistall tool. Further investigation of the WOB revealed that the (averaged) wearflat forces were reduced for the model with the tool, because of contraction of the tool during axial stick. At the same time, the cutting forces were increased by application of the tool. These two observations indicated that the tool caused an increased drilling efficiency, resulting in a higher ROP for the same (averaged) WOB.

The presented results indicated that the antistall tool increased the ROP, and insight into the working principle of the tool was obtained. On the basis of the results presented in this work, it was, however, not possible to draw definitive conclusions about the effectiveness of the tool in mitigating (torsional) stick/slip oscillations. A more detailed analysis of the latter observation can be found in Vromen (2015). Further research is required for the in-depth analysis of the effect of the tool in mitigating torsional stick/slip vibrations.

Acknowledgment

We acknowledge productive discussions with Nils Reimers on the functionality of the antistall tool.

References

Aarsnes, U. J. and Aamo, O. 2016. Linear Stability Analysis of Self-Excited Vibrations in Drilling Using an Infinite Dimensional Model. *J Sound Vib* **360** (C): 239–259. https://doi.org/10.1016/j.jsv.2015.09.017.

Aarsnes, U. J. and van de Wouw, N. 2018. Dynamics of a Distributed Drill String System: Characteristic Parameters and Stability Maps. *J Sound Vib* **417:** 376–412. https://doi.org/10.1016/j.jsv.2017.12.002.

Akutsu, E., Rødsjø, M., Gjertsen, J. et al. 2015. Faster ROP in Hard Chalk: Proving a New Hypothesis for Drilling Dynamics, Presented at the SPE/IADC Drilling Conference and Exhibition, SPE/IADC 173068, London, UK, 17–19 March. SPE-173068-MS. https://doi.org/10.2118/173068-MS.

Besselink, B., van de Wouw, N., and Nijmeijer, H. 2011. Semi-Analytical Study of Stick-Slip Oscillations in Drilling Systems. *J Comput Nonlinear Dynam* **6** (2): 021006-1–021006-9. https://doi.org/10.1115/1.4002386.

Besselink, B., Vromen, T., Kremers, N. et al. 2015. Analysis and Control of Stick-Slip Oscillations in Drilling Systems. *IEEE Trans Control Syst Technol* **24** (5): 1582–1593. https://doi.org/10.1109/TCST.2015.2502898.

Depouhon, A. and Detournay, E. 2014. Instability Regimes and Self-Excited Vibrations in Deep Drilling Systems. *J Sound Vib* **333** (7): 2019–2039. https://doi.org/10.1016/j.jsv.2013.10.005.

Detournay, E. and Defourny, P. 1992. Phenomenological Model for the Drilling Action of Drag Bits. *Int J Rock Mech Min Sci* **29** (1): 13–23. https://doi.org/10.1016/0148-9062(92)91041-3.

Detournay, E., Richard, T., and Shepherd, M. 2008. Drilling Response of Drag Bits: Theory and Experiment. *Int J Rock Mech Min Sci* **45** (8): 1347–1360. https://doi.org/10.1016/j.ijrmms.2008.01.010.

Dupriest, F. E. and Koederitz, W. L. 2005. Maximizing Drill Rates With Real-Time Surveillance of Mechanical Specific Energy. Presented at the SPE/IADC Drilling Conference, Amsterdam, The Netherlands, 23–25 February. SPE-92194-MS. https://doi.org/10.2118/92194-MS.

Germay, C., Denoël, V., and Detournay, E. 2009a. Multiple Mode Analysis of the Self-Excited Vibrations of Rotary Drilling Systems. *J Sound Vib* **325** (1–2): 362–381. https://doi.org/10.1016/j.jsv.2009.03.017.

Germay, C., van de Wouw, N., Sepulchre, R. et al. 2009b. Nonlinear Drillstring Dynamics Analysis. *SIAM J Appl Dyn Syst* **8** (2): 527–553. https://doi.org/10.1137/060675848.

Haughom, P. O. and Reimers, N. 2006. Torque Converter for Use When Drilling With a Rotating Drill Bit. Patent WO 2006/075921 A1.

Kjøglum, S. 2007. *Analysis of Down Hole Tools for Drilling Optimization*. MSc thesis, Norwegian University of Science and Technology, Department of Petroleum Engineering and Applied Geophysics, Trondheim, Norway.
Liu, X., Vlajic, N., Long, X. et al. 2013. State-Dependent Delay Influenced Drill String Dynamics and Stability Analysis. Presented at the ASME 2013 International Design Engineering Technical Conferences and Computers and Information in Engineering Conference, Portland, OR, 4–7 August. DETC2013-12904. https://doi.org/10.1115/DETC2013-12904.
Nandakumar, K. and Wiercigroch, M. 2013. Stability Analysis of a State Dependent Delayed, Coupled Two DOF Model of Drill-String Vibration. *J Sound Vib* **332** (10): 2575–2592. https://doi.org/10.1016/j.jsv.2012.12.020.
Reimers, N. 2012. Antistall Tool Reduces Risk in Drilling Difficult Formations. *J Pet Technol* **64** (1): 26–29.SPE-0112-0026-JPT. https://doi.org/10.2118/0112-0026-JPT.
Reimers, N. 2014. Mitigation of Torsional Vibrations and Stick-Slip Induced by Aggressive, Energy Efficient Drill-Bits. In *Third International Colloquium on Nonlinear Dynamics and Control of Deep Drilling Systems*, eds. E. Detournay, V. Denoël, N. van de Wouw et al., 9–14. Minneapolis: University of Minnesota.
Richard, T., Germay, C., and Detournay, E. 2007. Simplified Model to Explore the Root Cause of Stick-Slip Vibrations in Drilling Systems With Drag Bits. *J Sound Vib* **305** (3): 432–456. https://doi.org/10.1016/j.jsv.2007.04.015.
Selnes, K., Clemmensen, C., and Reimers, N. 2009. Drilling Difficult Formations Efficiently With the Use of an Antistall Tool. *SPE Drill & Compl* **24** (4): 531–536. SPE-111874-PA. https://doi.org/10.2118/111874-PA.
Vromen, T. 2015. *Control of Stick-Slip Vibrations in Drilling Systems*. PhD thesis, Eindhoven University of Technology, Eindhoven, The Netherlands.
Zhou Y. and Detournay E. 2014. Analysis of the Contact Forces on a Blunt PDC Bit, Presented at the 48th US Rock Mechanics/Geomechanics Symposium, Minneapolis, Minnesota, 1–4 June. ARMA 14-7351.

Appendix A—Numerical Algorithm Benchmark Model

Here, we outline the algorithm used to integrate the system of equations governing the response of the drillstring model. To simplify the exposition, we restrict the description of the numerical integration procedure to the benchmark model. The equations governing the dynamics of this model can be derived from Eqs. 21 through 24 for the model with an antistall tool, by setting the parameters describing the downhole tool to $\eta_b = 0$, $\gamma_b = 0$, $m_* = 0$, $\imath = 0$, and $\alpha = 0$, with the latter condition resulting in $\nu = \infty$ and $\kappa = \infty$ (but noting that $\nu/\kappa = 0$). With the constraints $u = u_b$ and $\varphi = \varphi_b$, and after summing Eqs. 21 and 22, the dynamical Eqs. 21 through 24 reduce to

$$u'' + \gamma u' + \eta^2 u = -\psi h(\tau;\tau_n) + \psi\lambda g(u') \quad \text{(A-1)}$$

$$\varphi'' + \varphi = -h(\tau;\tau_n) + \beta\lambda g(u') \quad \text{(A-2)}$$

$$\varphi(\tau) - \varphi(\tau - \tau_n) + \omega_0\hat{\tau}_n = 0, \quad \text{(A-3)}$$

with

$$h(\tau;\tau_n) = n(u(\tau) - u(\tau - \tau_n) + v_0\hat{\tau}_n) \quad \text{(A-4)}$$

and

$$\hat{\tau}_n = \tau_n - \tau_{n0}, \quad \tau_{n0} = \frac{2\pi}{\omega_0 n}, \quad \text{(A-5)}$$

$$\lambda = n\lambda_n. \quad \text{(A-6)}$$

Eqs. A-1 through A-6 are numerically integrated for three regimes of drilling: (1) normal drilling ($u' > -v_0$, $\varphi' > -\omega_0$), (2) axial stick ($u' = -v_0$, $u'' = 0$, $\varphi' > -\omega_0$), and (3) axial and torsional stick ($u' = -v_0$, $u'' = 0$, $\varphi' = -\omega_0$, $\varphi'' = 0$). Other regimes exist in principle but either are not judged to be physically justified (torsional stick without axial stick that would imply penetration of the bit without rotation), or are considered as rare events that cause the code to be aborted (backward rotation corresponding to $\varphi' < -\omega_0$ and bit bouncing corresponding to $d < 0$).

Normal Drilling. The Euler explicit method is used to numerically integrate Eqs. A-1 and A-2 after first transforming them into a set of four first-order differential equations. The solution is advanced over a timestep $\Delta\tau$ using

$$\begin{aligned}
u(\tau + \Delta\tau) &= u(\tau) + u'(\tau)\Delta\tau,\\
u'(\tau + \Delta\tau) &= u'(\tau) - [\gamma u'(\tau) + \eta^2 u(\tau) + \psi h(\tau;\tau_n)]\Delta\tau,\\
\varphi(\tau + \Delta\tau) &= \varphi(\tau) + \varphi'(\tau)\Delta\tau,\\
\varphi'(\tau + \Delta\tau) &= \varphi'(\tau) - [\varphi(\tau) + h(\tau;\tau_n)]\Delta\tau,
\end{aligned} \quad \text{(A-7)}$$

where the delay perturbation $\hat{\tau}_n$ is calculated according to Eq. A-3. The wearflat term was dropped because $g(u') = 0$ under normal drilling conditions ($u' > -v_0$, $\varphi' > -\omega_0$).

Axial Stick. The unilateral nature of the wearflat/rock contact is required to detect the time τ_{ak} at which the bit axial velocity vanishes. Thus, if the bit velocity is computed to be negative at the new time $\tau + \Delta\tau$ [i.e., if $u'(\tau + \Delta\tau) + v_0 < 0$ while $\varphi'(\tau + \Delta\tau) + \omega_0 > 0$] τ_{ak} is estimated as

$$\tau_{ak} = \tau + \frac{u'(\tau) + v_0}{[\gamma u'(\tau) + \eta^2 u(\tau) + \psi h(\tau;\tau_n)]}. \quad \text{(A-8)}$$

At time τ_{ak}, both the axial acceleration and the contact axial force are discontinuous, but $(u'' - \psi\lambda\tilde{g}) = 0$ where $[f(\tau)] = f(\tau^+) - f(\tau^-)$ and $\tilde{g}(\tau) := g(u'(\tau)$. According to Eq. A-1, applied at $\tau = \tau_{ak}$,

$$u''(\tau_{ak}) - \psi\lambda\tilde{g}(\tau_{ak}) = -\psi h(\tau_{ak};\tau_n) - \eta^2 u(\tau_{ak}) + \gamma v_0, \quad \text{(A-9)}$$

noting that both terms of Eq. A-9 are continuous at $\tau = \tau_{ak}$. Because $\tilde{g}(\tau_{ak}^-) = 0$,

$$u''(\tau_{ak}^-) = -\psi h(\tau_{ak}; \tau_n) - \eta^2 u(\tau_{ak}) + \gamma v_0. \quad \text{(A-10)}$$

In principle, there are two possible solutions at $\tau = \tau_{ak}^+$: either axial stick characterized by $u''(\tau_{ak}^+) = 0$ and $\tilde{g}(\tau_{ak}^+) \in [0, 1]$, or loss of contact at the wearflat/rock interface characterized by $u''(\tau_{ak}^+) < 0$ and $\tilde{g}(\tau_{ak}^+) = 1$. Axial stick occurs at τ_{ak} if

$$u''(\tau_{ak}^-) > -\psi\lambda, \quad \text{(A-11)}$$

in which case,

$$\psi\lambda\tilde{g}(\tau_{ak}^+) = -u''(\tau_{ak}^-). \quad \text{(A-12)}$$

[The stick condition (Eq. A-11) is derived from the requirement that $\tilde{g}(\tau_{ak}^+) < 1$]. If the condition of stick (Eq. A-11) is not satisfied, there is loss of contact at the wearflat/rock interface, with the bit acceleration $u''(\tau_{ak}^+) < 0$ given by

$$u''(\tau_{ak}^+) = u''(\tau_{ak}^-) + \psi\lambda. \quad \text{(A-13)}$$

However, the stick condition (Eq. A-11) is usually met. As long as $0 < \tilde{g}(\tau) < 1$ with $\tau > \tau_{ak}$, the bit remains in axial stick and the bit rotation is advanced using

$$\begin{aligned} &\varphi(\tau + \Delta\tau) = \varphi(\tau) + \varphi'(\tau)\Delta\tau, \\ &\varphi'(\tau + \Delta\tau) = \varphi'(\tau) - [\varphi(\tau) + h(\tau; \tau_n) - \beta\lambda\tilde{g}(\tau)]\Delta\tau, \end{aligned} \quad \text{(A-14)}$$

with

$$\tilde{g}(\tau) = \frac{\eta^2}{\psi\lambda}[u(\tau_{ak}) - v_o(\tau - \tau_{ak})] - \frac{\gamma v_0}{\psi\lambda} + \frac{n}{\lambda}[u(\tau_{ak}) - u(\tau - \tau_n) - v_o(\tau - \tau_{ak} - \hat{\tau}_n)]. \quad \text{(A-15)}$$

The bit exits axial stick to enter the normal drilling regime during a timestep if $\tilde{g}(\tau + \Delta\tau) < 0$. The slip time τ_{ap} can be estimated by linearly interpolating $\tilde{g}(\tau)$ over the timestep. To reinitiate the axial dynamics, $u'(\tau + \Delta\tau)$ and $u''(\tau + \Delta\tau)$ are set as

$$u''(\tau + \Delta\tau) = -\psi\lambda\tilde{g}(\tau + \Delta\tau), \quad u'(\tau + \Delta\tau) = -\psi\lambda\tilde{g}(\tau + \Delta\tau)(\tau + \Delta\tau - \tau_{ap}), \quad \tau < \tau_{ap} \leq \tau + \Delta\tau, \quad \text{(A-16)}$$

with a correction to the torsional solution caused by resetting $\tilde{g}(\tau + \Delta\tau) = 0$. Thus, advancing the solution for the next timestep is conducted using Eq. A-7.

Axial and Torsional Stick. A torsional stick event is detected if $\varphi'(\tau + \Delta\tau) + \omega_0 < 0$. The torsional stick time $\tau_{\omega k}$ $(\tau < \tau_{\omega k} < \tau + \Delta\tau)$ is then assessed from

$$\tau_{\omega k} = \tau + \frac{\varphi'(\tau) + \omega_0}{[\varphi(\tau) + h(\tau; \tau_n)]}. \quad \text{(A-17)}$$

It is assumed that the bit is completely immobile at $\tau = \tau_{\omega k}^+$. Backward rotation is unlikely because the (negative) acceleration needs to overcome a jump in frictional torque, noting also that the frictional torque associated with a backward rotation of the bit is proportional to the full weight on bit. Because it is assumed that $u'(\tau_{\omega k}^+) = -v_o$, there is generally a Dirac singularity in the force transmitted at the bit/rock interface at time $\tau = \tau_{\omega k}$.

During the stick phase, there is a torque buildup in the drillpipes because of continued rotation at the rig. Torsional slip then takes place at $\tau = \tau_{\omega p}$ when the applied torque balances the cutting and frictional torque. Because it is possible that the bit remains in axial slip at $\tau = \tau_{\omega p}$, $\tilde{g}(\tau_{\omega p})$ is calculated from equilibrium considerations because the cutting forces at $\tau = \tau_{\omega p}$ are identical to their values at $\tau = \tau_{\omega k}^-$; that is, $h(\tau_{\omega p}, \tau_n) = h(\tau_{\omega k}, \tau_n)$, noting that $\tau_n(\tau_{\omega p}) = \tau_n(\tau_{\omega k}) + \tau_{\omega p} - \tau_{\omega k}$. Thus,

$$\varphi(\tau_{\omega p}) = -h(\tau_{\omega k}, \tau_n) + \beta\lambda\tilde{g}(\tau_{\omega p}) \quad \text{(A-18)}$$

with

$$\varphi(\tau_{\omega p}) = \varphi(\tau_{\omega k}) - \omega_0(\tau_{\omega p} - \tau_{\omega k}). \quad \text{(A-19)}$$

Hence, the time of slip is given by

$$\tau_{\omega p} = \tau_{\omega k} + \frac{1}{\omega_0}[\varphi(\tau_{\omega k}) + h(\tau_{\omega k}, \tau_n) - \beta\lambda\tilde{g}(\tau_{\omega p})]. \quad \text{(A-20)}$$

If the solution is calculated at each timestep $\Delta\tau$, then acceleration $\varphi''(\tau + \Delta\tau)$ with $\tau < \tau_{\omega p} \leq \tau + \Delta\tau$ is given by

$$\varphi''(\tau + \Delta\tau) = \omega_0(\tau + \Delta\tau - \tau_{\omega p}), \qquad \tau < \tau_{\omega p} \leq \tau + \Delta\tau. \quad \text{(A-21)}$$

Appendix B—Parameters of the Drillstring Model Including Antistall Tool

The parameters of the drillstring model including an antistall tool are given here. The parameters are determined on the basis of the properties of a real drilling system. The parameters related to the bit/rock interaction are given in **Table B-1,** and those pertaining to the mechanical properties of the drillstring model and the properties of the antistall tool (i.e., lead, lead angle, axial spring stiffness, and damping in the tool) are listed in **Table B-2.**

Parameter	Symbol	Value	Unit
Drill-bit radius	α	0.16	m
Specific energy	ε	60	MPa
Wearflat length	ℓ	$1.2{\cdot}10^{-3}$	m
Contact stress	$\overline{\sigma}$	60	MPa
Cutting-face orientation	ζ	0.6	—
Bit-geometry parameter	ξ	1	—
Friction coefficient	μ	0.6	—
Number of blades	n	6	—

Table B-1—Bit parameters for the model with the antistall tool included.

Parameter	Symbol	Value	Unit
Steel density	ρ_s	8000	kg/m^3
Steel shear modulus	G	77	GPa
Steel elasticity modulus	E	200	GPa
Drillpipe length	L_p	8013.5	m
Length BHA below AST	L_b	44.6	m
Length BHA above AST	L_{hp}	229.2	m
Drillpipe outer radius	r_{po}	0.084	m
Drillpipe inner radius	r_{pi}	0.075	m
Heavy drillpipe outer radius	r_{hpo}	0.84	m
Heavy drillpipe inner radius	r_{hpi}	0.057	m
AST outer radius	r_{bo}	0.106	m
AST inner radius	r_{bi}	0.036	m
AST helix radius	r_h	0.081	m
Lead angle	θ	$\pi/4$	rad
Lead	$p = \tan(\theta) * 2\pi r_h$	0.509	m
Constraint constant	$\alpha = \frac{p}{2\pi}$	0.081	m
Drillpipe mass	$M_p = \rho\pi(r_{po}^2 - r_{pi}^2)L_p$	$2.88{\cdot}10^5$	kg
Heavy drillpipe mass	$M_{hp} = \rho\pi(r_{hpo}^2 - r_{hpi}^2)L_{hp}$	$2.19{\cdot}10^5$	kg
BHA below AST mass	$M_b = \rho\pi(r_{bo}^2 - r_{bi}^2)L_b$	$1.11{\cdot}10^4$	kg
Effective mass	$M = \frac{4}{\pi^2}M_p + M_{hp}$	$1.39{\cdot}10^5$	kg
Area cross section pipe	$A_p = \pi(r_{po}^2 - r_{pi}^2)$	$4.49{\cdot}10^{-3}$	m^2
Area cross section BHA	$A_{hp} = \pi(r_{hpo}^2 - r_{hpi}^2)$	$1.19{\cdot}10^{-2}$	m^2
Area cross section AST	$A_b = \pi(r_{bo}^2 - r_{bi}^2)$	$3.12{\cdot}10^{-2}$	m^2
Drillpipe inertia	$I_p = \rho L_p\frac{\pi}{2}(r_{po}^4 - r_{pi}^4)$	1827.4	kg·m^2

Table B-2—Drillstring parameters for the model with the AST included.

Parameter	Symbol	Value	Unit
BHA above AST inertia	$I_{hp} = \rho L_{hp} \frac{\pi}{2} (r_{hpo}^4 - r_{hpi}^4)$	113.0	kg·m^2
BHA below AST inertia	$I_b = \rho L_b \frac{\pi}{2} (r_{bo}^4 - r_{bi}^4)$	69.8	kg·m^2
Effective inertia	$I = \frac{4}{\pi^2} I_p + I_{hp}$	853.6	kg·m^2
Drillpipe torsional stiffness	$C_p = \frac{GJ_p}{L_p}$	273.9	(N·m)/rad
Drillpipe axial spring	$K_b = \frac{EA_p}{L_p}$	$1.12{\cdot}10^5$	N/m
AST axial spring stiffness	K_b	$9.5{\cdot}10^5$	N/m
AST axial damping	D_b	$14.3{\cdot}10^3$	(N·s)/m
Drillstring axial damping	D	$67.7{\cdot}10^3$	(N·s)/m

Table B-2 (continued)—Drillstring parameters for the model with the AST included.

Thijs Vromen is a design engineer of system dynamics at ASML, Veldhoven, The Netherlands. His research interests include modeling, analysis, and control of nonlinear systems. Vromen holds a MSc degree in mechanical engineering from the Eindhoven University of Technology and a PhD degree in mechanical engineering from the same university for his thesis on control of stick/slip vibrations in drilling systems.

Emmanuel Detournay is the T. W. Bennett Chair Professor in the Department of Civil, Environmental, and Geo-Engineering at the University of Minnesota. Before joining the university, he was a senior research scientist at Schlumberger Cambridge Research in England. Detournay's expertise is in petroleum geomechanics, with a current research focus on drilling mechanics—bit/rock interaction, self-excited drilling vibrations, drillstring/borehole interaction, and directional drilling.

Henk Nijmeijer is a full professor at Eindhoven University of Technology, and chairs the Dynamics and Control group. He holds MSc and PhD degrees from the University of Groningen, The Netherlands. Nijmeijer has authored or coauthored a large number of journal and conference papers, as well as several books, and is or was on the editorial board of numerous journals. He is currently the scientific director of the Dutch Institute of Systems and Control, Delft, The Netherlands.

Nathan van de Wouw is a full professor at the Eindhoven University of Technology. He also holds an adjunct full professor position at the University of Minnesota, and a (part-time) full professor position at the Delft University of Technology, The Netherlands. van de Wouw has held visiting-professor positions at the University of Santa Barbara, USA; the University of Melbourne, Australia; and the University of Minnesota. His current research interests are the modeling, model reduction, dynamic analysis, and control of nonlinear and delay systems, with applications to drilling systems—in particular, vibration mitigation, directional drilling, and managed-pressure drilling. van de Wouw has authored or coauthored more than 200 technical-journal and conference papers and two books. He is currently an associate editor for the journals *IEEE Transactions on Control Systems Technology* and *IEEE Transactions on Automatic Control*. In 2015, van de Wouw received the IEEE Control Systems Technology Award in recognition of his work toward the development and application of variable-gain control techniques for high-performance motion systems. He earned an MSc degree (with honors) and a PhD degree, both in mechanical engineering, from the Eindhoven University of Technology.